Check for updates

APPLIED PHYSICS

Capillary ratchets activated by interfacial flows for versatile torque generation and microassembly

Zhe Li[1,2], Keliang Liu[1], Lida Pan[1], Zhangyuan Cheng[3], Shuxian Li[2], Chengchen Guo[3], Jan G. Korvink[4], Jiadong Li[1]*, Yongbo Deng[4]*, Zongmin Ma[2]*, Cheng Zeng[1]*

Copyright © 2026 The Authors, some rights reserved; exclusive licensee American Association for the Advancement of Science. No claim to original U.S. Government Works. Distributed under a Creative Commons Attribution NonCommercial License 4.0 (CC BY-NC).

Chiral microstructures exhibit distinctive mechanical, electrical and optical properties, but reliable methods to generate unidirectional rotation with precise control remain limited. Previously, Zeng *et al.* developed "capillary machines," macroscopic machines with hollow channels that braid microscale wires into specific topologies using interfacial capillary forces. Here, we report a versatile ratcheting mechanism that is flow rate dependent. Under high–flow rate conditions, robust unidirectional rotation of the floating object is generated by the interplay between interfacial flows and capillary forces. Simulations reveal that interfacial flows depend on the actuation direction, leading to the observed hysteresis. Leveraging this principle, we successfully braid multiple microwires into a hierarchically twisted bundle without destructive torsion. By coupling interfacial hydrodynamics with geometric design, this approach establishes a scalable strategy for fabricating delicate chiral architectures, opening transformative paradigms in interface-mediated microassembly.

Downloaded from https://www.science.org at KIT Library on August 14, 2026

INTRODUCTION

The controlled generation of unidirectional rotation underlies fundamental processes across biology, physics, and engineering, from bacterial propulsion by flagellum (*1*, *2*) and viral genome packaging by molecular motors (*3*, *4*) to the work cycles of engines (*5*). Recent years have witnessed an explosion of research interest in harnessing external energy to precisely control unidirectional spin of micro- and nanomachines (*6*–*9*). Interfaces provide a natural platform for such conversion because they confine the motion of objects to two dimensions through pinning (*10*). By applying imbalanced in-plane forces, torque can be generated.

A number of interfacial strategies for unidirectional rotation generation have been developed in recent years. Spinners with polar designs can be fueled by chemical approaches such as bubbles generated from catalytic reactions (*11*–*13*) or Marangoni flows produced by dissolution of surfactants (*14*, *15*). Such chemical propulsion strategies are applicable to a wide range of systems, from colloidal particles (*11*) to macroscopic spinners (*14*). Yet chemical reactions are fundamentally spontaneous, thus difficult for active control, and ultimately limited by reactant consumption. Physical approaches, including the use of electric fields (*16*, *17*), optical fields (*18*), magnetic fields (*7*, *19*), and waves (*8*) offer more interactive and programmable routes to create ratchets but often require complex setups.

Capillary forces, which scale linearly with the length of the contact line, are an important driving force for manipulation and assembly across length scales (*10*). Capillary actions have long been used for adaptive assembly (*20*–*22*) and active transportation (*23*–*29*). Lately, capillary repulsion is emerging as a versatile, noncontact, and precise micromanipulation method (*30*–*34*). Since they originate from the tendency to minimize interfacial deformations, capillary forces are intrinsic to the interfaces (*10*, *35*). Thus, the object to be manipulated does not need to be responsive to external fields, which is typically required in some other contactless manipulation methods (*36*–*38*).

Zeng *et al.* previously invented "capillary machines:" simple 3D-printed devices that have hollow channels to shape the meniscus at the air-water interface and precisely control the position, orientation, and interplay of floating objects (the "floats") across length scales via repulsive capillary forces (*30*, *32*). When placed at the air-water interface surrounded by the channel wall, the float has one or multiple locations and orientations that minimize the surface energy. By prescribing the channel boundary, the capillary forces applied onto the float(s) can be programmed to achieve object manipulation. Taking advantage of contact angle hysteresis, the team further realized a "capillary ratchet" that converts the cyclic vertical motion of the device into net unidirectional rotation of the float. The behavior of the float has been described to satisfaction by a quasi-static model that assumes the float is always in an equilibrium configuration at any given water level.

Here, we present a previously unknown regime: A capillary ratchet that is activated by interfacial flows. For this class of machines, ratcheting effect emerges only when the device is actuated rapidly across the air-water interface. Interfacial flow created at such high speed deviates the float rotation from a quasi-static fashion, thus breaking time-reversal symmetry and generating torque efficiently. We harness this phenomenon for hierarchical twisting of microfibers that resemble the configurations of Litz wires (*39*–*41*). Notably, the symmetry breaking happens within the same channel, making this approach suitable for efficient twisting without introducing lateral tension from the fibers. Beyond revealing a mechanism for unidirectional rotation, this approach opens pathways toward future delicate interfacial manipulation, force measurement, and assembly.

[1]Key Laboratory of Multifunctional Nanomaterials and Smart Systems, Suzhou Institute of Nano-tech and Nano-bionics (SINANO), Chinese Academy of Sciences (CAS), Suzhou 215123, P.R. China. [2]School of Mechanical Engineering, Dalian University, Dalian 116600, P.R. China. [3]School of Engineering, Westlake University, Hangzhou 310030, P.R. China. [4]Institute of Microstructure Technology (IMT), Karlsruhe Institute of Technology (KIT), Hermann-von-Helmholtzplatz 1, Eggenstein-Leopoldshafen 76344, Germany.
*Corresponding author. Email: jdli2009@sinano.ac.cn (J.L.); yongbo.deng@kit.edu (Y.D.); mazongmin@dlu.edu.cn (Z.M.); czeng2024@sinano.ac.cn (C.Z.)

RESULTS

Conversion of vertical channel motion into in-plane float motion

Our aim is to manipulate floating objects in a dynamically programmed fashion by applying repulsive capillary forces via an evolving boundary.

To this end, we design devices with hollow channels of varying boundary shapes over the vertical direction. We use 3D printing to fabricate the plastic devices and plasma treatment to render the channel surface hydrophilic. The device is then placed in a water bath, where the meniscus near the boundary curves up. By controlling the wettability of the float, repulsive capillary forces arise between the boundary and the float (*10*, *35*), which determines the position and orientation of the float.

When the device is actuated vertically, the meniscus moves to different levels inside the channel and thus varies its shape. This creates dynamic repulsive capillary forces that move the floats. To actuate the device vertically, we build a motorized actuation apparatus (Fig. 1, A and B). The 3D-printed device is mounted to the stage and placed in the water bath. The vertical movement is controlled by a programmable electric motor.

The cross section of the float used here takes the shape of a windmill toy. The device is also custom designed to have a central channel with the same windmill-shaped horizontal cross section that is linearly scaled up from the float. By design, the channel takes a helical shape: The cross section of the channel is rotated along a vertical centerline by 180° over the height of the device (Fig. 1C). When partially filled with water, the air/water interface will assume the shape of the device wall at that water level. The interface can be approximately considered to have a windmill shape that curves up along its periphery to wet the hydrophilic device wall. In reality, the three-phase contact line does not remain in the same horizontal 2D plane due to pinning, yet we have previously used a 2D approximation of the contact line, which leads to a satisfactory agreement with experimental observations (*30*).

We place a 3D-printed float of the same plastic material at the air-water interface. As the plastic is denser than water, the float pins the interface down and the water-plastic contact angle appears greater than 90°. The float is thus trapped at the center of the channel thanks to capillary repulsions (*35*). When a windmill-shaped float is placed at the interface, its equilibrium orientation aligns with the channel wall (Fig. 1B, inset).

We rotate the float by vertically actuating the device across the air/water interface in a programmed fashion. When the meniscus adapts to the channel boundary at a new height, the capillary repulsion increases. Therefore, a torque is generated on the float and rotates it. We mark the float with red and blue regions for visualization purposes. For each given program, we track the vector connecting the center points of the red and blue regions so that the rotation angle can be plotted as a function of time (Fig. 1D).

In a typical program, the starting point is a low position where most of the device is submerged under the interface except the top approximately 1 mm. The device is then moved up to a position where only approximately 1 mm at the bottom of the device remains in water, held for up to 10 s for the float motion to stabilize, moved back down to the starting point, and held for another few seconds to complete one cycle. We also let the system run continuously and record data over multiple cycles for statistics.

The capillary ratchet activated by interfacial flows

We first operate the device for one cycle at a vertical speed of 160 mm/min and observed reversible float rotations (Fig. 2A and movie S1). The float displays a quasi-static behavior: It rotates by close to 180° at a steady rotation rate when the device moves up and reverses that process when the device moves down. The total helical design of the channel is 180°, and the float rotations deviate slightly from 180° and −180° because the channel height is not fully used in the experiment. We tracked the rotation angle (φ) over time and observed zero net rotation after one cycle is complete.

A ratchet (i.e., a net rotation in one cycle) emerges with the same float and device at a vertical actuation speed of 4800 mm/min (Fig. 2B

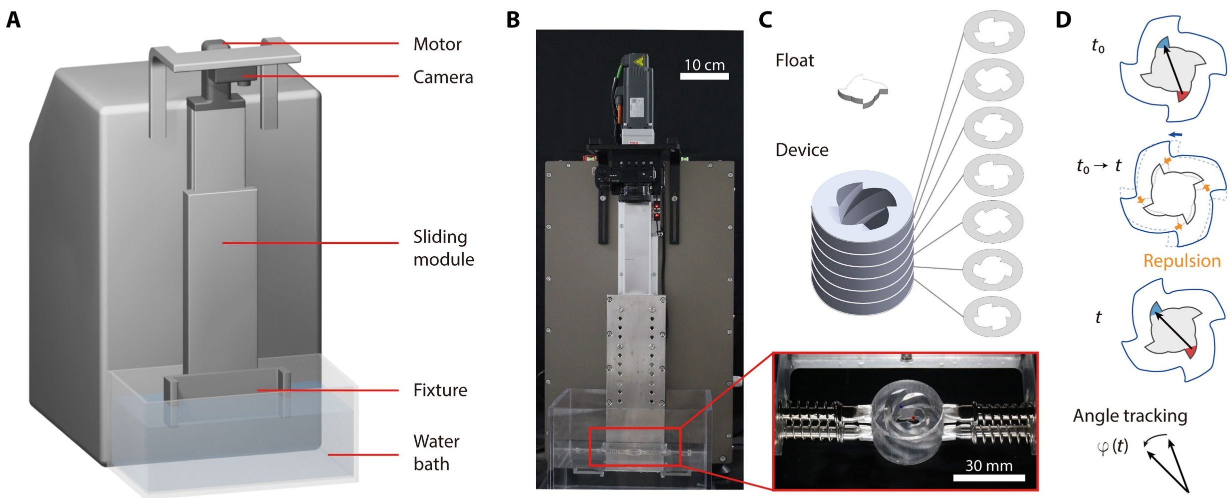

Fig. 1. Design and operation of the apparatus. (**A**) A 3D rendering of the actuation apparatus, including a motorized stage, a camera for video recording, a sliding module, a fixture to hold the device, and a water bath. (**B**) A photo of the setup. Inset: a device mounted on the fixture and placed in the water bath with a float at the center of the interface. We design mounting holes as anchoring points on the outside of each device and use spring-loaded stainless-steel pins to fix the device while actuating its vertical motion. (**C**) The device is designed with an open helical channel that has a windmill-shaped cross section at any height. The windmill shape is evenly rotated along its height for a total of 180°, as depicted by the cross sections. A float with the same windmill-shaped cross section is shown as an example. (**D**) At any given time t_0, with a given static device boundary, the float rests at a referred orientation. As the boundary rotates, repulsive capillary forces (shown in orange arrows) arise, which generate a torque on the float. The float eventually equilibrates to a new orientation. We mark two opposite sides of the float in red and blue respectively so that the float rotation angle (φ) can be tracked as a function of time by the digital imaging system.

Downloaded from https://www.science.org at KIT Library on August 14, 2026

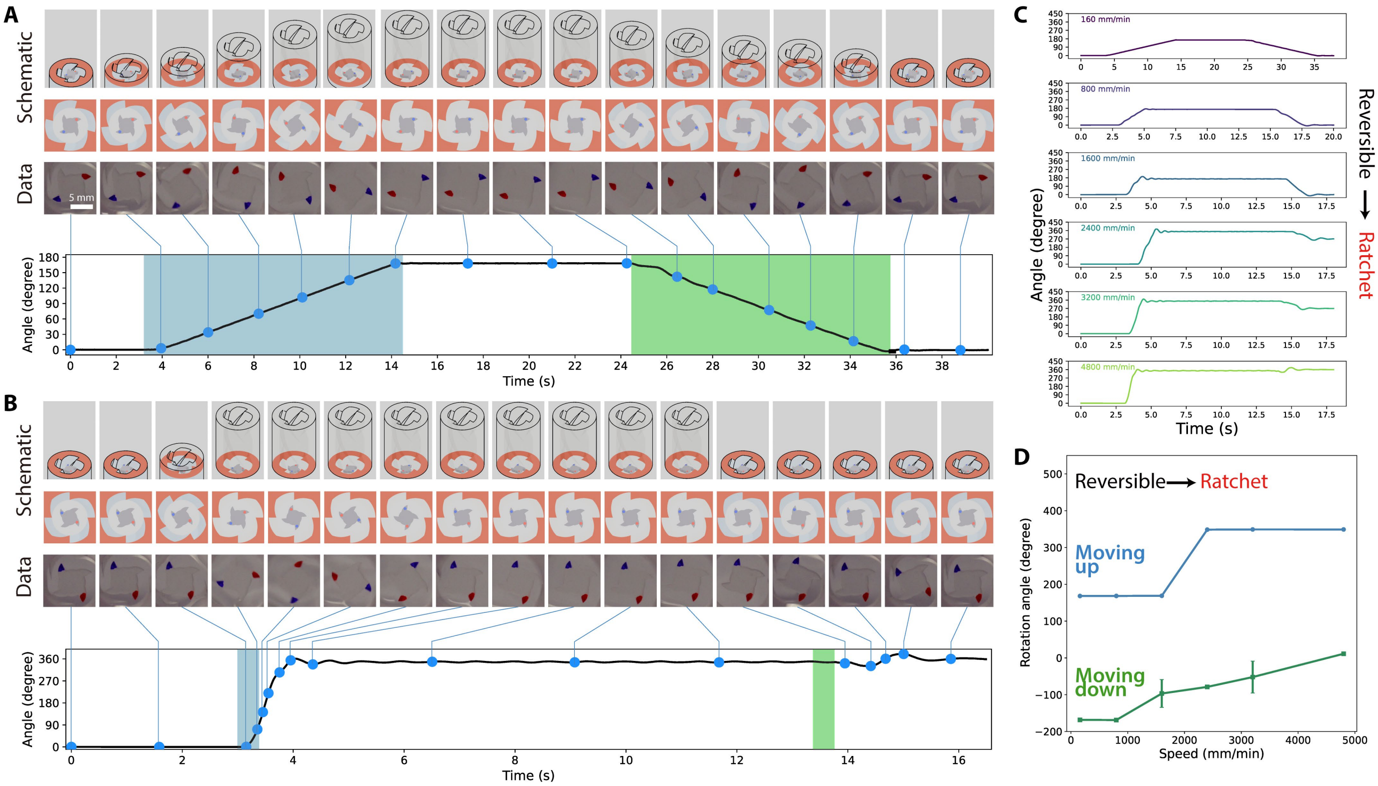

Fig. 2. The ratcheting effect activated by high actuation speeds. (**A**) Snapshots of a rotating float (top) and its rotation angle over time (bottom) in one cycle at a low actuation speed. The device is moved up at a speed of 160 mm/min (highlighted by light blue background), held for 10 s, and then moved back down to its origin at the same speed (highlighted by light green background). The float follows the rotation of the windmill-shaped cross section of the device and shows 0 net rotation in one cycle. Scale bar, 5 mm. (**B**) Results of a float at a high actuation speed. The device is moved up at a speed of 4800 mm/min (highlighted by light blue background), held for 10 s, and then moved back down to its origin at the same speed (highlighted by light green background). The float shows a delayed rotation and an "overshoot" in rotation angle in the first half. (**C**) More angle tracking data at varied speeds. A clear time reversal symmetry breaking is observed when the speed is increased from 1600 to 2400 mm/min. (**D**) The average rotation angle from 10 individual cycles plotted with respect to actuation speed. Error bars represent the standard deviation. Device movement direction (up or down) is also marked by color. A shift from 180° to 360° is observed for the up cycle, and from −180° to 0° is observed for the down cycle. Collectively, they lead to the increase in net rotation angles.

and movie S2). Unlike the previous case, the time-reversal symmetry is broken. When the device moves up, the float rotation "overshoots": It rotates by approximately 360°, while the channel only has 180° in the helical design. Such overshoot has not been observed in previous capillary machines. In addition, the rotation continues after the device motion, as highlighted by the blue background shadings in the figure, has stopped. On the contrary, when the device moves down, the float rotation "undershoots": It oscillates but does not show a net rotation, insensitive to the helical design. To this end, we have successfully created a flow-dependent ratchet in which inertia plays an important role.

Both the "overshoot" in angle and delayed response in rotation suggest that the system can no longer be described by the quasi-static approximation. Our hypothesis is that the float behavior is the result from capillary forces coupled with the flow field generated in the high flow rate regime.

Speed is a key control knob to the transition in regime. We further study the impact of speed with more granularity (Fig. 2C). By plotting out the angle versus time curves, we observe no net rotation in one cycle up to an actuation speed of 1600 mm/min. Beyond this speed, the float rotates more on the up stroke and less on the down stroke, which collectively lead to the breaking of the time reversal symmetry.

For statistics, we track the floats over 10 cycles, and summarize the average forward and backward rotation angles and the standard deviations (Fig. 2D). A clear transition from reversible to ratchet is again observed at the speed of 1600 mm/min, despite that the rotation angle under the same conditions is not always identical. In addition, all rotation angles are close to multiples of 90°, in agreement with the C4 rotational symmetry of the windmill-shaped cross section.

On a static interface, i.e., when the actuation rate is zero, the float orientation is purely set by the capillary force balance. This is also true at low actuation rates, when the meniscus can be treated quasi-statically (*30*). Thus, the float orientation aligns with the channel cross section. However, when the actuation rate exceeds 1600 mm/min, the float rotation angle no longer aligns with the channel, although it still stops at an equilibrium orientation that matches the channel orientation when the device motion ends. It is thus tempting to assume that the symmetry breaking at high actuation rate is due to interfacial flows that overcome capillary forces.

We rationalize the regime transition from the low speed to high speed conditions by analyzing the relevant dimensionless numbers: the Reynolds number (*Re*), Weber number (*We*), and capillary number (*Ca*) for all situations. A characteristic length L = 17 mm, averaged from the inner and outer diameter of the channel cross section,

Downloaded from https://www.science.org at KIT Library on August 14, 2026

is used. Properties of water under room temperature are used, including dynamic viscosity $\mu = 0.89 \times 10^{-3}$ Pa · s, density $\rho = 997$ kg/m^3, and surface tension coefficient $\gamma = 72.8$ mN/m. The actuation speed of the stage is used as the characteristic velocity V. The results are summarized in table S1.

Re is defined as $Re = \frac{\rho V L}{\mu}$. On the basis of the calculations, it ranges from 50.7 to 1521.6, when the speed increased from 160 to 4800 mm/min. The relatively high *Re* suggests that inertial forces dominate over viscous forces.

We further calculate *We*, which represents the relative strength between capillary forces and inertial forces. Under the 160 mm/min actuation, *We* is 8.6×10^{-3}, which is small and capillary force dominate. At 1600 mm/min where we start to see the transition experimentally, *We* is 0.086, two orders of magnitude higher than the case above. At 4800 mm/min, which is the highest speed tested, *We* is 0.775, close to the order of unity. Since $We = \frac{\rho V^2 L}{\gamma}$, it increases quickly with respect to the characteristic velocity.

We note that the transition of regime happens below $We = 1$. This is because of the simplified choice of the characteristic dimension used for calculations. The channel geometry can contribute to the critical transition value of *We*. The helical channel structure is not well described by the dimensionless number calculations, yet it plays a critical role in promoting interfacial secondary flows. The contribution from this geometric effect helps the system to overcome the surface tension effects at a *We* smaller than 1.

The hysteresis is not unique to the specific operating parameters mentioned above. The pause time between the up strokes and down strokes can be tuned. We observe this hysteresis under varied pause times, albeit more variations are observed among the repeated tests when the pause time is reduced to zero (fig. S1). It is also interesting to note that the up stroke and down stroke are independent (fig. S2). For instance, it is possible to operate the device in the quasi-static regime on the up stroke and in the ratcheting regime on the down stroke. On the way up, the float will show a 180° rotation as in Fig. 2A; on the way down, the float will show a 0° rotation as in Fig. 2B. This feature allows tunable rotation angles from each cycle via controlled operations.

Interfacial flow simulations

For a deeper understanding on the origin of the ratcheting effect, we further simulate the dynamic evolution of the liquid/vapor interface at the center of the device channel during its vertical motion. The fluid flow is simulated without the float to avoid the high computational cost and numerical errors caused by the moving mesh arisen from the float motion. Nevertheless, simulations of the fluid per se would provide valuable insights on the interfacial flows, which are critical to the symmetry breaking. We use the phase-field method to analyze the interfacial flow because it enables accurate capture of the evolution of two-phase interfaces and is widely applied to track the diffuse interface between immiscible fluids.

We use the Navier-Stokes equations to resolve mass and momentum transport in the central channel fluid, while also accounting for the non-negligible effects of surface tension in this system. The Navier-Stokes equations can thus be expressed as

$$\rho\frac{\partial \mathbf{u}}{\partial t} + \rho(\mathbf{u}\cdot\nabla)\mathbf{u} = \nabla\cdot\left[-p\mathbf{I} + \mu\left(\nabla\mathbf{u} + (\nabla\mathbf{u})^{\mathrm{T}}\right)\right] + \mathbf{F}_{\mathrm{st}} + \rho\mathbf{g} \quad (1)$$

where ρ is the fluid density (kg/m^3), μ is the dynamic viscosity (N·s/m^2), $\boldsymbol{u}$ is the velocity field (m/s), p is the pressure (Pa), $\boldsymbol{I}$ is the identity tensor, $\boldsymbol{g}$ is the gravitational acceleration vector (m/s^2), and $\boldsymbol{F}_{\mathrm{st}}$ is the surface tension force acting at the liquid/vapor interface.

The surface tension force is defined as

$$\boldsymbol{F}_{\mathrm{st}} = \sigma\delta\kappa\mathbf{n} \quad (2)$$

where $\boldsymbol{n}$ is the unit normal to the interface, σ is the surface tension coefficient (N/m), $\kappa = -\nabla\cdot\boldsymbol{n}$ is the curvature, and δ is the Dirac delta function, which is nonzero only at the interface.

To enforce the contact angle at solid boundaries, an additional boundary force was included

$$\mathbf{F}_\theta = \sigma\delta\left(\boldsymbol{n}_{\mathrm{wall}}\cdot\mathbf{n} - \cos\theta_{\mathrm{w}}\right)\mathbf{n} \quad (3)$$

where θ is the prescribed contact angle and $\boldsymbol{n}_{\mathrm{wall}}$ is the unit normal to the wall. For strictly no-slip boundaries, the velocity at the wall vanishes and the contact angle cannot be explicitly imposed, while the interface remains pinned. Allowing for finite slip permits the specification of a contact angle. This feature was implemented using a wetted wall coupling condition, which constrains the wall-normal velocity component

$$\mathbf{u}\cdot\boldsymbol{n}_{\mathrm{wall}} = 0 \quad (4)$$

In addition, a frictional boundary force was applied

$$\mathbf{F}_{\mathrm{fr}} = -\frac{\mu}{\beta}\mathbf{u} \quad (5)$$

where β is the slip length, chosen to be equal to the mesh element size. Through this boundary condition, the equilibrium contact angle θ between the fluid interface and the solid wall could be prescribed.

The two-phase flow dynamics are governed by the Cahn-Hilliard equation, which we use to track the diffuse interface between two immiscible fluids. The interface is defined by the variation of the dimensionless phase-field variable ϕ from -1 to 1. For numerical implementation, the Cahn-Hilliard equation is split into two coupled equations

$$\frac{\partial\phi}{\partial t} + \mathrm{u}\cdot\nabla\phi = \nabla\cdot\frac{\gamma\lambda}{\varepsilon^2}\nabla\psi \quad (6)$$

$$\psi = -\nabla\cdot\varepsilon^2\nabla\phi + \left(\phi^2 - 1\right)\phi \quad (7)$$

where $\boldsymbol{u}$ is the fluid velocity (m/s), γ is the mobility (m^3·s/kg), λ is the mixing energy density (N), and ε (m) is the interfacial thickness parameter. The auxiliary variable ψ is introduced for computational convenience. The relation between the mixing energy density, interfacial thickness, and the surface tension coefficient σ is given by

$$\sigma = \frac{2\sqrt{2}}{3}\frac{\lambda}{\varepsilon} \quad (8)$$

Typically, the interfacial thickness parameter is set as $\varepsilon = h_c/2$, where h_c is the characteristic mesh size across the interface. The mobility γ controls the timescale of Cahn-Hilliard diffusion and must be carefully chosen: It should be large enough to maintain the interfacial thickness but sufficiently small to avoid excessive suppression of convective effects. A common initial estimate is $\gamma = \varepsilon^2$. In this model, we use a relatively large mobility to ensure correct pressure variations across the interface.

Within the phase-field framework, the volume fractions of the two fluids are defined as

$$V_{f1} = \frac{1-\phi}{2} \quad (9)$$

Downloaded from https://www.science.org at KIT Library on August 14, 2026

$$V_{f2} = \frac{1+\phi}{2} \tag{10}$$

Here, we define air as fluid 1 and water as fluid 2. The density (kg/m^3) and viscosity (Pa·s) of the mixture are smoothly interpolated across the interface using

$$\rho = \rho_w + \left(\rho_{air} - \rho_w\right) V_{f2} \tag{11}$$

$$\mu = \mu_w + \left(\mu_{air} - \mu_w\right) V_{f2} \tag{12}$$

where subscripts w and air denote the properties of water and air, respectively.

We specify the boundary conditions as follows: The bottom and sidewalls of the container are defined as wetted boundaries, while the top surface is set as a zero-pressure boundary. The lower half of the container is initially filled with water to represent our experimental conditions. The device walls are also treated as wetted boundaries, with a prescribed contact angle imposed at these surfaces. Note that this contact angle is varied depending on the device moving direction to represent the dynamic contact angles. We use a small receding contact angle and a large advancing angle to closely mimic the experiments. Furthermore, the device is implemented with a moving mesh to reproduce the experimental procedure with high fidelity.

We perform numerical simulations for both upward and downward strokes of the device actuated across the liquid/vapor interface at 4800 mm/min, yielding the corresponding fluid flow fields at the channel center (Fig. 3A and movie S3). A clear hysteresis is observed. On the up stroke, a counterclockwise vortex builds up over time on the interface (Fig. 3B), in agreement with the observed "overshoot." On the down stroke, however, the interfacial flow is concentrated at the four corners while the central part of the interface shows nearly zero flow (Fig. 3C). In addition, a close-up check will show that the arrows close to the corners are curved downward, suggesting that the interfacial flow turns into the axial flow. The results are in alignment with the "undershoot." Collectively, we observe the hysteresis from the interfacial flows which resemble the float behavior.

The simulation results are also supported by flow visualization with tracer particles dispersed at the interface (movies S1 and S2). In the steady state, the particles form a cluster at the center of the meniscus due to capillary attraction. We then move the device at same rates as the conditions of the float experiments. At low actuation speeds, particles rotate collectively as a cluster both on the up and down strokes. At high actuation speeds, the cluster shows rapid rotation when the device is moved up and almost no rotation when the device is moved down, closely resembling the hysteresis observed in float experiments.

The simulations reveal a flow field that shows radial variations. We further test floats at increasing diameters while keeping thickness and material unchanged. We observe an increase in cumulative rotation angle for diameter up to 10 mm, beyond which the angle drops (Fig. 3D and movie S4). We further plot the average rotation angle and the variations from the individual cycles (Fig. 3E) and observe the same trend as Fig. 3D. Such results qualitatively resemble the flow field obtained from our simulation results. For the up stroke, a major vortex dominates within 10 mm, and flow rate increases with the distance from the center. Above 10 mm, the vortex is strongly distorted by the boundary. In addition, the corner flows on the down stroke start to play a role, leading to clockwise rotations. Therefore, the flow produces maximum acceleration to the float up to 10 mm.

Further simulations will be necessary to quantitatively predict the float behavior, which is beyond the scope of this work. Nevertheless, the simulations here provide a simplified view of the origin of the hysteresis to a reasonable degree.

On the basis of the experimental and computational evidence, we conclude that the hysteresis originates from interfacial flows. In the reversible regime, the actuation rate is small and the *We* is on the order of 10^{-4} to 10^{-2}. In this case, capillarity dominates, and the float rotates alongside the channel boundary. In the ratcheting regime, the actuation rate is large and the *We* is greater than the order of 10^{-2}. The helical channel wall also exerts a driving force to the fluid. Depending on whether the channel moves up or down, the tilted helical wall of the channel promotes or suppresses the secondary flow at the interface. Furthermore, the contact angle depends on whether the device moves up or down. The chiral design of the helix, together with the contact angle hysteresis, breaks the time reversal symmetry. The ratcheting effect is more pronounced at higher actuation speeds potentially due to greater contact angle hysteresis (*42*).

Generalization of the flow-activated capillary ratchet mechanism

The ratcheting effect is not unique to the windmill shaped channel and float. Instead, it can be generalized to a wide range of channel and float designs. We design floats to represent multiple levels of symmetry, from circle (with an infinitely high rotational symmetry), to square and windmill (with a C4 symmetry), to triangle (with a C3 symmetry), to rectangle and track (with a C2 symmetry). All floats share the same circumscribed circle.

Using the previous windmill channel, we first show that the ratcheting effect can be reliably reproduced for all other shapes of floats tested. In all cases, ratcheting occurs for 10 consecutive cycles. The windmill float has also been placed in a mirrored configuration and maintained the ratcheting behavior (fig. S3). Note that the selection of the float strongly influences the net rotation angle (Fig. 4A and movie S5).

The float with the highest rotation symmetry, the circular float, shows the highest cumulative rotation among all float configurations. The windmill-shaped float that matches the channel cross-section geometry shows the second largest cumulative rotation. Among the rest of floats, the triangle and the rectangle show greater net rotation than the square and the track.

We further isolated the angle versus time curves from each individual cycle (fig. S4). While the channel has a 180° rotation by design, all types of floats show an "overshoot" on the up stroke, and an "undershoot" on the down stroke. Most floats show rotation angles close to multiples of 90°, consistent with the four-quadrant design of the windmill-shaped channel cross section. The triangle has more varieties of final orientations due to its symmetry mismatch from the channel cross section.

In addition, we see multiple regimes on the curves. On each up stroke, the initial quick counterclockwise rotation is always followed by a "snap" event, which is a brief clockwise rotation. After that, the float oscillates until it reaches the equilibrium rotation angle.

The overshoot/undershoot and the snap/oscillation events are shape dependent. For the circular float, the initial spin is relatively gradual, followed by a long snap event and oscillations with a small

Downloaded from https://www.science.org at KIT Library on August 14, 2026

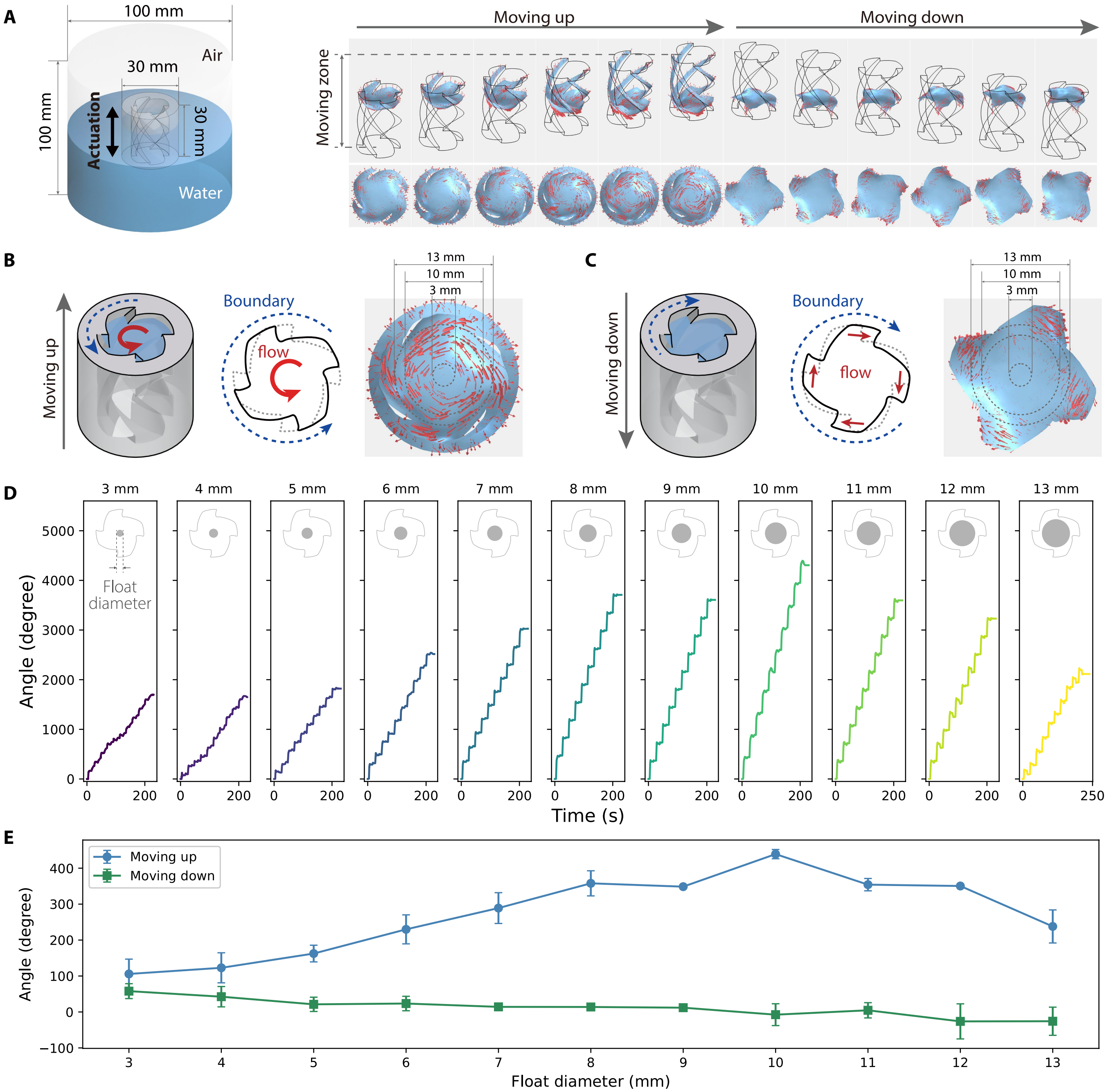

Fig. 3. Simulations of interfacial flow show hysteresis. (**A**) The setup of the finite element analysis includes a cylindrical space filled with air and water. The device is actuated vertically across the interface using a moving mesh to replicate the experiment at a high actuation speed. The float is omitted for simplicity of simulations. The tangential flow velocities (red arrows) are plotted at different water levels (blue) with both a perspective view and a top-down view. (**B** and **C**) Illustrations of the generated interfacial flow direction (red arrows) and the boundary rotation direction (blue arrows) when the device is moved up and moved down. The windmill-shaped boundary in its initial state (gray dashed line) and a rotated state (solid black line) are drawn to show the rotation direction. A representative snapshot of the flow velocity is shown, where concentric rings are drawn to demonstrate the length scale. (**D**) Cumulative experimental rotation angle of circular floats at different diameters (d) tracked over 10 cycles of device vertical motion and plotted with respect to time. The cumulative rotation angle increases with float diameter and peaks when $d = 10$ mm, after which the angle drops as d further increases. (**E**) A scatter plot of the average rotation angle from each cycle. Error bars represent the SDs of each group.

Downloaded from https://www.science.org at KIT Library on August 14, 2026

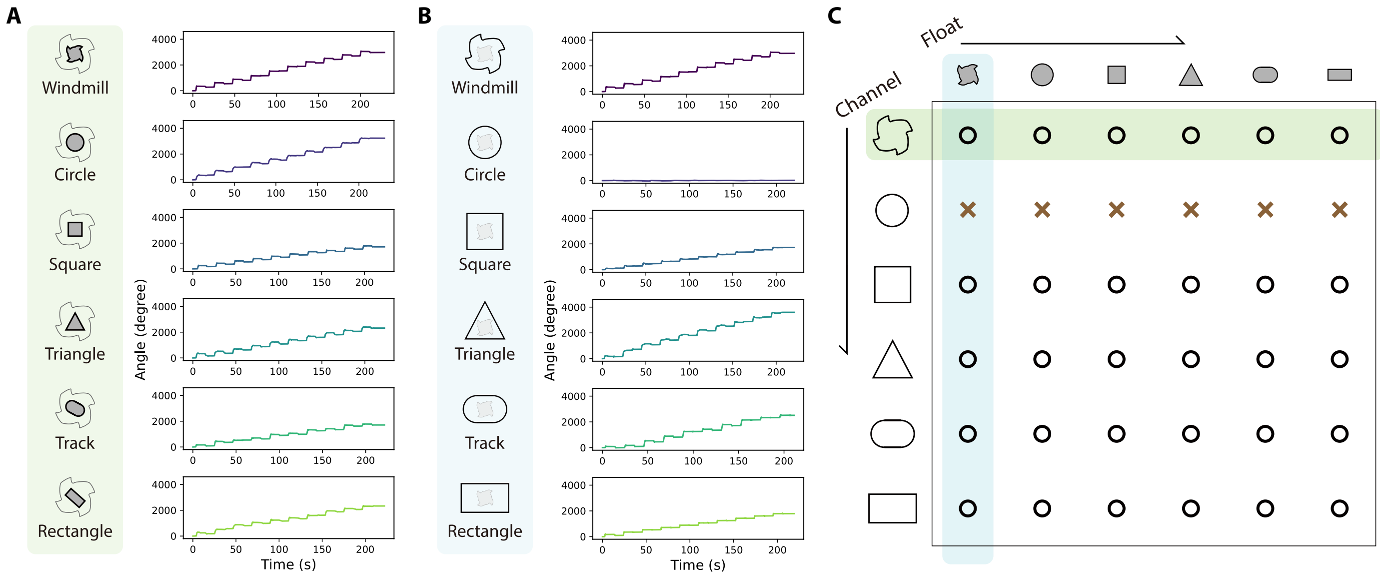

Fig. 4. Generalization of the ratcheting mechanism to alternative float and channel designs. (**A**) Floats with varied shapes are tested in a windmill-shaped channel, as depicted in green background. Rotation angles of the floats are tracked over 10 cycles and plotted cumulatively with respect to time. In each cycle, the device is moved up at a speed of 3200 mm/min, held for 10 s, moved down at the same speed, and held for another 10 s. While a ratcheting effect is observed for all floats, the degree of rotation is highly dependent on the shape of the float. (**B**) Channels with varied cross sections are used to actuate a windmill-shaped float, as depicted in blue background. The devices are actuated using the same program for 10 cycles, and the angle tracking data are plotted. Substantial rotation is observed for all cases except a circular channel cross section. (**C**) A table summarizing whether the ratchetting effect can occur (open black circles) or not (brown crosses) under arbitrary combinations of float and channel shapes.

amplitude. For all other floats, the initial rotation is faster, and the snap/oscillation is more pronounced.

We believe the following factors contribute to the shape-dependent rotation results: (i) how the float interacts with the boundary via capillary forces and (ii) how the float perturbs and couples with the flow field. Tentatively, we think that the circular and the windmill floats show the relatively largest rotation because their effective coupling with the flow field. Moreover, the circular float has the weakest coupling with the boundary via capillary forces thanks to its high symmetry. Thus, it is the least decelerated float by capillary repulsion, as demonstrated by the small snap and oscillations. The cumulative rotational angle is likely a compound effect from multiple factors. Thus, a universal quantitative explanation to the rotation angle is challenging.

We believe that the initial and final orientation of the float is set by capillary-driven alignment between the float and the channel cross section. Such capillary repulsion sets multiple minimum energy orientations separated by energy barriers in between. A static experimental analysis is performed to confirm the preferred orientations of floats (fig. S5). Therefore, although interfacial flows can drive the float to overcome energy barriers and overshoot, once the channel motion stops, the float is decelerated by such barriers which lead to the snap and oscillation events. The float eventually stops at an orientation that satisfies the shape alignment with the channel.

We further illustrate this angle-dependent energy landscape by simulations. In the dynamic simulations reported in the previous section, the float is omitted. Here, we perform static simulations with the float to better understand the interactions between the boundary and the float via capillary forces. The simulations are adapted from the previously reported general framework (*30*) to include the more complicated geometry used in this study. In brief, we scan the float at rotation multiple angles relative to the channel and calculate the energy of the system in each state. The simulations show an energy landscape that has a period of 90°, with minima that closely resemble the preferred orientations observed in experiments (fig. S6).

We expected floats with low symmetry to have certain preferred orientations and thus align with the channel wall when the device stops. However, the fact that the circular float also rotates by multiples of 90° is highly unexpected. In previously reported capillary machines, the float orientation is set by capillary-force-driven geometry. Following this principle, the capillary force acting on a circular float should be independent of its orientation due to its infinite rotational symmetry. Yet, we have shown that the circular float does have preferred orientations by repeatedly disturbing the float by tweezers and recording its equilibrium orientation (fig. S7). We have tested circular floats manufactured by 3D-printing (using two different resins) and computer numerical control (CNC) machining, and reproduced the same result. The preferred orientation for circular floats is likely caused by minor imperfections in float manufacturing that dominate the local three-phase contact line.

Optical and scanning electron micrographs confirm the existence of the microscale imperfections (fig. S8A). We also image the contact line with optical methods to demonstrate nonuniform pinning around the periphery. From optical imaging, we see reflections from certain locations of the interface near the edge of the float, suggestion high curvature regions due to pinning. From optical profilometry, we also observe abrupt height changes near the pinning sites (fig. S8B). As an additional test, we intentionally fabricate a float with a prescribed pinning site, a small 0.2-mm hump on the edge of a disk (*7*). Reflection from the interface confirms pinning at that point. This float also shows a clear orientation preference and ratcheting effect (fig. S9).

Downloaded from https://www.science.org at KIT Library on August 14, 2026

In addition to floats, we further generalize this mechanism to different channel designs. The same set of shapes is used for the channels, in combination with a windmill-shaped float (Fig. 4B). The strongest ratcheting is observed for the triangle channel, followed by windmill, track, and rectangle. The ratcheting effect breaks down in the channel with a circular cross section. The curves from individual cycles are again plotted separately (fig. S10 and movie S6), and similar characteristics are observed as the previous curves.

In addition, we have tested all possible channel-float combinations generated from the six types of fundamental shapes. We successfully demonstrate the ratcheting effect in almost all scenarios. The only exception is a cylindrical channel with a circular cross section, in which case no helical structure exists. We perform control experiments with the cylindrical channel and confirm no ratcheting effect regardless of actuation rate (fig. S11). The helical channel design is clearly vital for the ratchet.

We summarize the results in a table (Fig. 4C). Such results prove the versatility of our flow-activated ratcheting mechanism and enables flexible channel/float designs to meet application-specific needs.

We consider size as another key factor, in addition to shape. Scaling is critical for the application of the mechanism. To explore direct applications in the microscale, we miniaturize the channel and the float. The windmill-shaped device is downscaled to 30% of its original size to accommodate the small floats. We test two floats that are smaller than the ones mentioned above: (i) a 3D-printed circular float with a 2 mm diameter (fig. S12) and (ii) a Si cuboid which has a 131 by 272 μm cross section, cut from a wafer (fig. S13). Note that the surface area of the Si cuboid float is approximately 0.5% of the smallest float shown in Fig. 3. We operate the device using the same setup, and image the floats with an optical microscope. In both cases, we show clear evidence of the ratcheting behavior. Such results further expand the application of our approach to the micrometer scale and open doors to direct manipulation of microobjects.

The design of the helix, namely, the pitch and the total height, can be tuned as well. We test two sets of devices using the windmill cross section. First, we decrease the pitch to 50 and 20% of the original value while keeping the total height constant. The ratcheting effect is observed in all cases, and the device with a tighter pitch shows a greater cumulative rotation (fig. S14A). Second, we elongated the device to five times its original height while keeping the pitch constant. A greater cumulative rotation angle is also achieved (fig. S14B). Therefore, both pitch and height of the device are knobs to tune the rotation angle, and thus can be modified for designated needs.

Last, we verify the reproducibility of our system by 3D-printing identical devices and running parallel experiments (fig. S15). The intragroup and intergroup variations are within 10°. This is sufficient for applications such as twisting, where a 180° rotation is needed for one crossing. We envision that this variation can be further reduced by tightening the tolerance in fabrication.

Torque generation for microbraiding

Taking one more step toward controlled manufacturing, we establish a workflow to estimate the torque output using this mechanism. This is realized via analyzing the float motion in response to the flow. The angular acceleration α of the float is estimated by taking the second derivative of the rotation angle θ as a function of time t. The torque (τ) is then calculated via $\tau = I\,\alpha$, where I is the moment of inertia calculated from the geometry and density of the float. We take data in Fig. 3 as a sample dataset for the torque estimation (fig. S16) and find a maximum torque output on the order of 10^{-8} N · m. It is also highly related to experimental conditions (e.g., float size) and can be tuned accordingly. This torque is smaller than a macroscopic DC motor (on the order of 10^{-2} to 1 N · m) (*43*), yet much greater than the biological flagellar motor (on the order of 10^{-18} N · m) (*44*). It offers an effective means to output a net unidirectional torque that is in between the macroscopic world and the molecular world.

We further leverage the flexibility in channel/float design and demonstrate one application in the hierarchical twisting of microfibers. Such bundles are promising candidates for high-end surgical suture (*45*) and nano-Litz wires (*39*, *41*).

We tether microwires to the float for twisting, as demonstrated in our previous work (*30*, *32*). Here, we use silk fibers with individual diameters ranging from 10 to 20 μm fabricated by dry spinning. During each experiment, the fibers are attached to the same float. The capillary ratchet is cycled vertically to generate torque on the float, which drives the fibers to twist (Fig. 5A). The free end of the fibers is fixed to an anchor to avoid unwinding.

To demonstrate the capability of the ratchet, we prepare hierarchical structures twisted in two levels. In this case, we make a 4 by 4 bundle: we first twist four fibers counterclockwise in each bundle of level 1 (L1), and then attach four L1 bundles to one float and twist them clockwise in level 2 (L2) to achieve the final structure (Fig. 5B). Note that the rotation direction (i.e., clockwise or counterclockwise) can be customized via channel helical design (fig. S17). We use scanning electron microscopy (SEM) to confirm the structure of the final bundle (Fig. 5C).

This ratchet is self-limiting. As twisting proceeds, the fibers get increasingly taut. As torque accumulates in the twist, the cumulative rotation of the float eventually plateaus. For instance, the ratchet effect vanishes after 50 cycles, at which point the torque output is balanced by the mechanical stress stored in the twisted bundle (movie S7). This is in fact an important feature for braiding at this length scale as we can tune the maximum torque to prevent over twisting or mechanical damages to the fibers.

Hierarchical microbraiding via integrated ratchets

We lastly add one more knob to control the microstructures: We integrate multiple functional segments in one device and activate them sequentially over time via programmed vertical motion of the device. As a demonstration of this mechanism, we design an integrated device for hierarchical twisting (Fig. 6A). This device is composed of two channels on top for L1 counterclockwise twisting, a merging channel, and one channel at the bottom to rotate the combined float clockwise for L2 twisting. We use two rectangular floats that can assemble into a larger rectangular float. On each level, the floats display the ratcheting effect as designed.

We make a 2 by 2 bundle with silk fibroin fibers with this device as a demonstration. First, we repeatedly cycle the device in the top L1 region to ensure two fibers are twisted in each pair. Later, we move the device up and let the two floats, embedded with magnetic beads, to stably attach to each other. Last, we repeatedly cycle the device in the bottom region to complete the L2 twisting (Fig. 6B and movies S8 and S9). By SEM, we confirm that a 2 by 2 bundle is formed, which has a structure that closely resembles the rendering (Fig. 6C and fig. S18).

Hierarchical twists are widely used in mechanical and electric engineering (*40*, *45*), and here we provide a simple and versatile way to generate them at the microscale. Industrial braiding machines

Downloaded from https://www.science.org at KIT Library on August 14, 2026

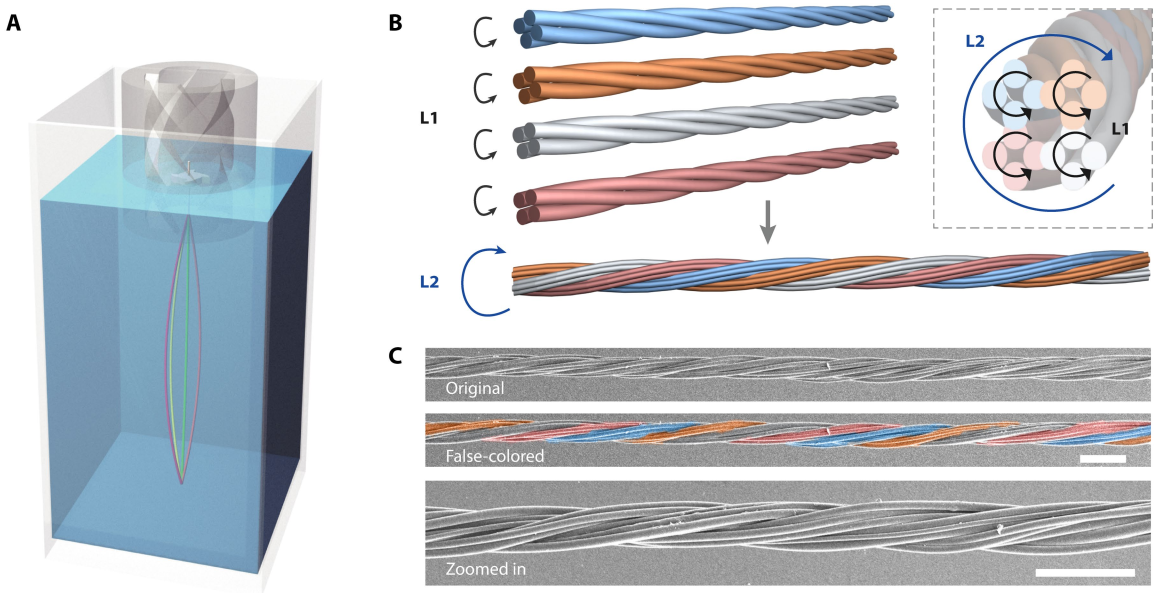

Fig. 5. Hierarchical twisting with the flow-activated capillary ratchet. (**A**) A 3D rendering of the setup used for twisting. The top end of the individual wires is attached to a needle pierced through the float, while the other end is attached to an anchor in the water bath. (**B**) A 3D rendering of the hierarchical twisting structure. Four individual fibers are first twisted counterclockwise to form Level 1 bundles (L1). Four L1 bundles are then twisted in the opposite direction to form the Level 2 bundle (L2). A cross section of the final bundle is depicted in the inset. (**C**) Representative SEM images of the final bundle at two different magnifications; scale bars, 200 μm. The SEM image is false colored to better illustrate the hierarchical twisting of fibers. The same color is used for fibers within each L1 bundle.

(*46*) are not applicable in making such braids at the micrometer scale because the fibers tend to break under high mechanical stress. Alternative microbraiding machines that are proposed typically require delicate apparatus (*41*, *47*) or complicated mechanical design (*48*, *49*). Self-assembly–based approaches exist, yet they are mostly limited to certain patterns (*50*, *51*). In contrast, we offer a technique with a self-limiting torque control, a flexible modular design, and low manufacturing cost, which enables scaling up via parallel operation of multiple devices using the same control stage. Depending on the specific need, the number of hierarchies, the number of fibers in each hierarchy, and the twisting direction can all be precisely engineered. Our approach provides the flexibility to make any hierarchical twists by tuning the channel design in combination with the actuation program.

DISCUSSION

We have demonstrated a capillary ratchet that is activated by interfacial flows. While reversible behavior occurs at low actuation rates, the time reversal symmetry is broken at high actuation rates while the float remains within the same channel. Using experiment and finite element analysis, we reveal the critical role of interfacial flow in symmetry breaking. We have also demonstrated the versatility of this mechanism by generalizing the float and channel designs to anything except a cylindrical channel.

The flow-activated capillary ratchets are unique in that they use nothing but a moving interface to control the rotational symmetry breaking of the float. The float and channel walls do not touch each other; instead, they are coupled via the meniscus. Therefore, we achieve great flexibility over the floats to be manipulated: They can take a wide range of materials, shapes, and dimensions.

With such understandings, we showcase the capability of harnessing the torque generated to output work at the microscale. We provide a universal, efficient, and green solution for all microscale braiding applications. Beyond silk fibers, our method can in principle braid any fiber material into hierarchical twists. By using conductive component wires at the micrometer or submicrometer scale, we can fabricate micro- or nanobraids (micro-/nano-Litz wires) that hold great practical significances in high-bandwidth low-loss interconnects among servers in data centers (*39*). The versatility also makes our approach particularly attractive for braiding multifunctional surgical suture (*45*, *52*) and artificial muscle (*53*, *54*). We have estimated the torque generated by this phenomenon, which can guide future applications. For instance, we envision that the mechanical work needed to fabricate a microbundle can be estimated from the bundle structure (e.g., pitch, fiber diameter, and topology) and the material properties (e.g., Young's modulus). We can design the peak torque by tuning the channel and float designs and the actuation speed accordingly to ensure the self-limiting braiding of an intended structure.

We also consider our approach as a general mechanism for the conversion between linear translation and unidirectional rotation at the millimeter to micrometer scale that can be applied beyond twisting. Such a mechanism holds potential in many other applications, such as interfacial energy harvesting from wave power (*55*), droplet mixing in droplet microfluidics (*56*), rheology testing of microscale samples (*57*), or as actuators in micromachines and soft robotics (*7*, *19*).

MATERIALS AND METHODS

Design and fabrication of capillary ratchet machine

We used SolidWorks 2020 (SolidWorks Corporation) to create the 3D models of the ratchet devices. Channels were made by using the Swept Cut function on a solid cylinder. The channel cross-section designs can be found in the Supplementary Materials (fig. S19). We used a Form 4 3D printer with Clear V5 clear photopolymer resin

Downloaded from https://www.science.org at KIT Library on August 14, 2026

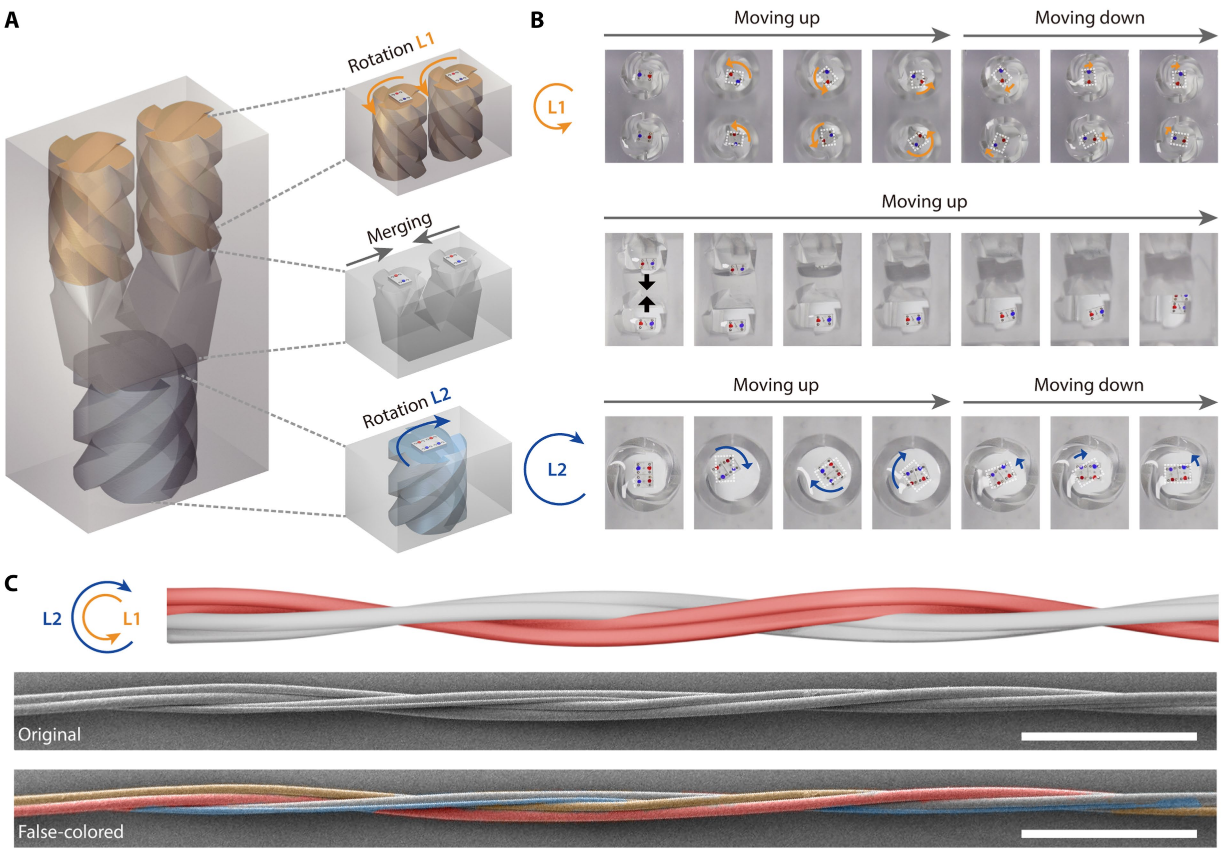

Fig. 6. Hierarchical twisting with integrated ratchets. (**A**) A 3D rendering demonstrating the design of the integrated ratchet. It has three functional segments: Rotation L1 (colored in orange), for rotating two individual floats in one direction; merging, for combining the two floats embedded with magnetic beads; and rotation L2 (colored in blue), for rotating the combined float in the opposite direction. (**B**) Snapshots of floats monitored in the individual functional segments are shown. Rectangles with white dashed lines are drawn to represent the float orientation in the previous snapshot, while colored arrows demonstrate the direction of float motion since the previous snapshot. Clear ratcheting effects are observed in both L1 and L2. (**C**) A 3D rendering and SEM images of a 2 by 2 hierarchical twist. Two fibers are attached to each individual float and twisted in this device. A hierarchical twisted bundle is successfully formed by first cycling the device through the rotation L1 segment for forty times, then elevating the device through the merging segment, then cycling the device through the rotation L2 segment for sixty times. The structure of the bundle is confirmed by SEM; scale bars, 500 μm. The SEM image is also false colored to better illustrate the individual fibers.

(Formlabs) to fabricate ratchet machines with a typical layer thickness of 100 μm. After printing, the device was placed together with the 3D printer's build platform into a cleaning machine (Form Wash, Formlabs) and washed with isopropyl alcohol for 20 min at high speed to remove excess resin. Following the wash, the device was transferred to an ultraviolet curing chamber (Form Cure, Formlabs) and cured for 3 min at 35°C to ensure complete polymerization of the resin. The cured device was then ready for subsequent experiments. We measured the contact angles on this material to be 68°.

Design and fabrication of the floats

We designed the floats using SolidWorks 2020. The geometric designs of all floats can be found in the Supplementary Materials (fig. S20). The floats were 3D printed following the same procedure as the devices unless stated otherwise.

For the circular floats, two additional fabrication methods were used. We used a custom-formulated hydrophobic photocurable resin to fabricate circular floats using a different 3D printer (ELEGOO, Saturn 4 Ultra), yielding floats with a contact angle of 100°. In addition, we produced circular Teflon floats by mechanically cutting Teflon plates by a CNC, with a measured contact angle of 106°. For all floats, two opposite points were marked red and blue, respectively, to serve as markers for subsequent rotation tracking via color-based recognition.

Actuation apparatus and its operation

We controlled the vertical motion of the ratchet by a custom-built apparatus, which consists of four main components: an imaging system, a motion control unit, a clamping mechanism, and a water bath. We assembled the water bath from 1-cm-thick acrylic sheets which measures 30 cm by 30 cm in length and width. Positioning holes are printed on the side of each device. Before each experiment, we fixed the ratchet device onto the apparatus by inserting the spring-loaded stainless-steel pins into the positioning holes. By programming the control unit, the vertical motion of the ratchet could be precisely executed. The apparatus allows for customizable control of the movement speed, stopping position, and pause duration, enabling the ratchet to perform predefined motion profiles.

Rotation angle data collection and processing

We used a ZV-E10 camera (Sony) mounted directly above the ratchet apparatus to record the rotational motion of the float. The camera orientation could be adjusted in four directions: X, Y, Z, and rotation (R).

Downloaded from https://www.science.org at KIT Library on August 14, 2026

During each experiment, we recorded the float motions at 1080p resolution and 120 frames per second for subsequent analysis.

We extracted rotational angle data using the OpenCV package in Python. In each frame of the video, the program identifies the red and blue markers on the float and constructs a directional vector between them. We then use this vector to quantify the rotation angle of the float over time.

System miniaturization

We fabricated the device following the same 3D-printing procedure as described above. The Si cuboids were cut from a wafer. To record the rotation the Si cuboids, we positioned a microscope (AOSVI, AO-3M180) with its lens directly above the device. To enhance visualization, we applied a horizontal light source at the air-water interface, which highlighted the Si cuboid float.

Characterization of the three-phase contact line for circular floats

We used two distinct methods to visualize the three-phase contact line of circular floats at the air-water interface. First, a circular float was placed at the interface and confined by a circular boundary device to maintain its stable position. An optical microscope (AOSVI, AO-3M180) was positioned directly above the float, supplemented by an external ring-shaped light-emitting diode light source to illuminate the air-water interface. The profile of the contact line surrounding the circular float was clearly visualized through the microscope, rendered by the reflected light from the interface.

Second, we used a 3D optical profiler (Sensofar S neox 090) to image the contact line of a 2-mm-diameter circular float. Similar to the first method, the float was spatially confined. Under the profiler, the air-water interface was first located using interference fringes, after which the lens was translated to the contact line region surrounding the float to take the precise topography of the contact line. This is a local approach that offers better vertical resolution yet a much reduced scan size compared with the first method.

Quasi-static simulations

We use a finite element method (FEM) to calculate the total energy of a system containing a float at the air-water interface. We followed the previously reported method (*30*) and set up the simulations in Python. The system consists of a shell-shaped container and a floating object, both represented as 3D STL meshes. The container and the float STL files were both sliced horizontally to obtain the channel interior boundary and the float cross-sectional geometry.

The total energy of the system comprises three contributions: (i) the capillary energy arising from the fluid interface deformation, calculated by solving the Young-Laplace equation using FEM on the 2D domain bounded by the container interior and float perimeters; (ii) the gravitational potential energy of the submerged float portion; and (iii) the work done by contact line forces at the container wall. The equilibrium vertical position Z_0 is determined by minimizing the total energy with respect to float height.

To investigate orientation-dependent behavior, the float was rotated in the horizontal plane from 0° to 360° in 1° increments, with the energy and equilibrium height computed at each orientation. The capillary length $L_c = 2.7$ mm was used. This approach reveals the preferred floating orientation (minimum energy state) and quantifies the energy landscape governing the alignment of the float inside the channel.

Flow visualization with tracer particles

To visualize fluid motion during device actuation, we dispersed polyethylene terephthalate (PET) particles with a diameter of 100 μm as tracer particles. We repeatedly transferred small quantities of PET with a laboratory spatula and gently deposited them onto the interface at the center of the channel until most of the open area was covered. As we actuate the ratchet device vertically, the movement of the particles on the interface was recorded to visualize the interfacial flows.

Computational fluid dynamics simulations

We used the finite element analysis software COMSOL Multiphysics to simulate the fluid dynamics at the channel center during device motion. We imported the STL file of the device into the software and define its position and the surrounding fluid domain accordingly. We used a moving mesh to simulate the device.

Torque estimation

The torque (τ) was estimated from the moment of inertia (I) and the angular acceleration (α) of the float via $\tau = I\ \alpha$. The moment of inertia was calculated based on the float density (1.18 g/cm^3 for the 3D-printed resin material) and dimensions. The angular acceleration was calculated by taking the second derivative of the float rotation angle with respect to time using numpy. A Gaussian filter was applied to the angle tracking data before taking the derivatives to reduce noise.

Preparation of dry-spun silk fibers

Natural silk fibers were degummed with a Na_2CO_3 solution and then dissolved in a 9.3 M LiBr solution. Following a 3-day dialysis and purification, a fresh 5.0% (w/v) silk fibroin aqueous solution was obtained.

Then, 30 ml of the freshly prepared regenerated silk fibroin solution [5 weight % (wt %)] was loaded in a 50-ml centrifuge tube. Glycerol (100 mg/ml) aqueous solution was added into the centrifuge tube sequentially to make the weight ratio of silk:glycerol = 75:20. The mixture solution was concentrated under vacuum at 30°C for 18 hours to obtain the spinning dope with a concentration of ~50 wt %.

Subsequently, the spinning dope was extruded through the needle (20 gauges) at a spinning rate of 5 to 10 mm/s to form solid silk fibers. Silk fibers were collected on a customized sample holder and stored in a chamber at 25 ± 2°C and 50 ± 5% relative humidity. The as-spun silk fibers were poststretched to 4× their original length in deionized water for subsequent use.

Stepwise hierarchical fiber twisting

We tethered the silk fibers to the float via an elastic needle. We first inserted a fine stainless-steel needle (diameter = 0.35 mm) into a small hole at the center of the float. We then glued the fibers to the free end of the needle. Last, we fixed the other end of the fibers to an anchor placed at the bottom of the water bath. The twisting process occurs entirely underwater. As the experiment proceeded, the fibers gradually twisted around each other and became increasingly taut.

We used a total of 16 fibers for the stepwise hierarchical twisting demonstration. We first divided the fibers into four groups, each containing four fibers. Within each group, the fibers were twisted counterclockwise. Once a group was twisted, we removed it from the water bath and fixed it onto a glass slide to preserve its twisted configuration before proceeding to the next group. After all groups were processed, we combined the twisted fiber bundles and conducted

Downloaded from https://www.science.org at KIT Library on August 14, 2026

an additional clockwise twisting step following similar procedures, thereby completing the hierarchical twisting of 16 fibers.

Hierarchical fiber twisting with integrated ratchets

We used integrated ratchets comprising three segments for hierarchical twisting of silk fibers. We used two rectangular floats embedded with magnetic beads and tethered fibers to the floats following the same procedure as above. We then began the twisting process by cycling the device in the upper segment (L1), where two individual floats, each tethered by two fibers, were rotated for 40 cycles. We then raised the device through the middle segment and allowed the two floats to merge. As the device rise, the two magnetic bead-embedded floats combined into a single unit. Last, we cycled the device in the bottom segment (L2) to rotate this newly formed composite float for 60 cycles to form the final twisted bundle.

Characterization of the twists

We characterized the morphology of the fibers using an SEM (Quanta 400). To prepare the sample for imaging, we fixed the two ends of the bundle onto a glass slide and deposited an approximately 10-nm-thick gold layer by sputter coating (Emitech K550X) to improve conductivity. We then image the samples under SEM in secondary electron mode at an accelerating voltage of 15 kV.

Supplementary Materials

The PDF file includes:
Supplementary Text
Figs. S1 to S20
Tables S1 and S2
Legends for movies S1 to S10

Other Supplementary Material for this manuscript includes the following:
Movies S1 to S10

REFERENCES

1. Y. Sowa, R. M. Berry, Bacterial flagellar motor. *Q. Rev. Biophys.* **41**, 103–132 (2008).
2. T. Drobnič, E. J. Cohen, T. Calcraft, M. Alzheimer, K. Froschauer, S. Svensson, W. H. Hoffmann, N. Singh, S. G. Garg, L. D. Henderson, T. R. Umrekar, A. Nans, D. Ribardo, F. Pedaci, A. L. Nord, G. K. A. Hochberg, D. R. Hendrixson, C. M. Sharma, P. B. Rosenthal, M. Beeby, In situ structure of a bacterial flagellar motor at subnanometre resolution reveals adaptations for increased torque. *Nat. Microbiol.* **10**, 1723–1740 (2025).
3. B. Prevo, W. C. Earnshaw, DNA packaging by molecular motors: From bacteriophage to human chromosomes. *Nat. Rev. Genet.* **25**, 785–802 (2024).
4. J. Kindt, S. Tzlil, A. Ben-Shaul, W. M. Gelbart, DNA packaging and ejection forces in bacteriophage. *Proc. Natl. Acad. Sci. U.S.A.* **98**, 13671–13674 (2001).
5. J. B. Heywood, *Internal Combustion Engine Fundamentals* (McGraw-Hill Education, New York, ed. 2, 2018).
6. H. Zhou, C. C. Mayorga-Martinez, S. Pané, L. Zhang, M. Pumera, Magnetically driven micro and nanorobots. *Chem. Rev.* **121**, 4999–5041 (2021).
7. W. Wang, J. Giltinan, S. Zakharchenko, M. Sitti, Dynamic and programmable self-assembly of micro-rafts at the air-water interface. *Sci. Adv.* **3**, e1602522 (2017).
8. J.-W. Barotta, S. J. Thomson, L. F. L. Alventosa, M. Lewis, D. M. Harris, Bidirectional wave-propelled capillary spinners. *Commun. Phys.* **6**, 87 (2023).
9. Y. Fan, H. Wu, J. Wang, J. Lv, Field-programmable topographic-morphing array for general-purpose lab-on-a-chip systems. *Adv. Mater.* **37**, 2410604 (2024).
10. P.-G. de Gennes, F. Brochard-Wyart, D. Quere, *Capillarity and Wetting Phenomena: Drops, Bubbles, Pearls, Waves* (Springer-Verlag New York, 2004).
11. D. P. Rivas, M. Sokolich, H. Muller, S. Das, Patchy bubble-propelled colloids at interfaces. *Adv. Mater. Interfaces* **10**, 2300226 (2023).
12. L. Liu, T. Bai, Q. Chi, Z. Wang, S. Xu, Q. Liu, Q. Wang, How to make a fast, efficient bubble-driven micromotor: A mechanical view. *Micromachines* **8**, 267 (2017).
13. A. M. Brooks, M. Tasinkevych, S. Sabrina, D. Velegol, A. Sen, K. J. M. Bishop, Shape-directed rotation of homogeneous micromotors via catalytic self-electrophoresis. *Nat. Commun.* **10**, 495 (2019).
14. S. W. Song, S. Lee, J. K. Choe, A. C. Lee, K. Shin, J. Kang, G. Kim, H. Yeom, Y. Choi, S. Kwon, J. Kim, Pen-drawn Marangoni swimmer. *Nat. Commun.* **14**, 3597 (2023).
15. G. Lu, G. Zhu, B. Peng, R. Zhao, F. Shi, M. Cheng, A multi-engine marangoni rotor with controlled motion for mini-generator application. *ACS Appl. Mater. Interfaces* **15**, 23980–23988 (2023).
16. J. Kedzierski, E. Holihan, Linear and rotational microhydraulic actuators driven by electrowetting. *Sci. Robot.* **3**, eaat5643 (2018).
17. A. Takei, K. Matsumoto, I. Shomoyama, Capillary motor driven by electrowetting. *Lab Chip* **10**, 1781–1786 (2010).
18. C. Maggi, F. Saglimbeni, M. Dipalo, F. De Angelis, R. Di Leonardo, Micromotors with asymmetric shape that efficiently convert light into work by thermocapillary effects. *Nat. Commun.* **6**, 7855 (2015).
19. G. Gardi, S. Ceron, W. Wang, K. Petersen, M. Sitti, Microrobot collectives with reconfigurable morphologies, behaviors, and functions. *Nat. Commun.* **13**, 2239 (2022).
20. N. Bowden, A. Terfort, J. Carbeck, G. M. Whitesides, Self-assembly of mesoscale objects into ordered two-dimensional arrays. *Science* **276**, 233–235 (1997).
21. B. Pokroy, S. H. Kang, L. Mahadevan, J. Aizenberg, Self-organization of a mesoscale bristle into ordered hierarchical helical assemblies. *Science* **323**, 237–240 (2009).
22. S. Li, B. Deng, A. Grinthal, A. Schneider-Yamamura, J. Kang, R. S. Martens, C. T. Zhang, J. Li, S. Yu, K. Bertoldi, J. Aizenberg, Liquid-induced topological transformations of cellular microstructures. *Nature* **592**, 386–391 (2021).
23. S. Feng, P. Zhu, H. Zheng, H. Zhan, C. Chen, J. Li, L. Wang, X. Yao, Y. Liu, Z. Wang, Three-dimensional capillary ratchet-induced liquid directional steering. *Science* **373**, 1344–1348 (2021).
24. L. Yang, W. Li, J. Lian, H. Zhu, Q. Deng, Y. Zhang, J. Li, X. Yin, L. Wang, Selective directional liquid transport on shoot surfaces of *Crassula muscosa*. *Science* **384**, 1344–1349 (2024).
25. X. Liu, M. Gao, B. Li, R. Liu, Z. Chong, Z. Gu, K. Zhou, Bioinspired capillary transistors. *Adv. Mater.* **36**, e2310797 (2024).
26. M. K. Chaudhury, G. M. Whitesides, How to make water run uphill. *Science* **256**, 1539–1541 (1992).
27. J. Lv, Y. Liu, J. Wei, E. Chen, L. Qin, Y. Yu, Photocontrol of fluid slugs in liquid crystal polymer microactuators. *Nature* **537**, 179–184 (2016).
28. B. Zhang, J. Li, J. Zhou, L. Chow, G. Zhao, Y. Huang, Z. Ma, Q. Zhang, Y. Yang, C. K. Yiu, J. Li, F. Chun, X. Huang, Y. Gao, P. Wu, S. Jia, H. Li, D. Li, Y. Liu, K. Yao, R. Shi, Z. Chen, B. L. Khoo, W. Yang, F. Wang, Z. Zheng, Z. Wang, X. Yu, A three-dimensional liquid diode for soft, integrated permeable electronics. *Nature* **628**, 84–92 (2024).
29. M. Prakash, D. Quere, J. W. M. Bush, Surface tension transport of prey by feeding shorebirds: The capillary ratchet. *Science* **320**, 931–934 (2008).
30. C. Zeng, M. W. Faaborg, A. Sherif, M. J. Falk, R. Hajian, M. Xiao, K. Hartig, Y. Bar-Sinai, M. P. Brenner, V. N. Manoharan, 3D-printed machines that manipulate microscopic objects using capillary forces. *Nature* **611**, 68–73 (2022).
31. G. Xie, P. Li, P. Y. Kim, P.-Y. Gu, B. A. Helms, P. D. Ashby, L. Jiang, T. P. Russell, Continuous, autonomous subsurface cargo shuttling by nature-inspired meniscus-climbing systems. *Nat. Chem.* **14**, 208–215 (2022).
32. A. Sherif, M. W. Faaborg, C. Zeng, M. P. Brenner, V. N. Manoharan, Braiding, twisting, and weaving microscale fibers with capillary forces. *Soft Matter* **20**, 3337–3348 (2024).
33. M. Delens, A. Franckart, D. M. Harris, N. Vandewalle, 3D-printed spines for programmable liquid topographies and micromanipulation. *Nat. Commun.* **16**, 4348 (2025).
34. J. Metzmacher, M. Delens, N. Vandewalle, Ring of capillary actuators as trap, tweezers and ratchet for floating particles. *Sci. Rep.* **15**, 20617 (2025).
35. D. Vella, L. Mahadevan, The "Cheerios effect". *Am. J. Phys.* **73**, 817–825 (2005).
36. A. Pal, M. Sitti, Programmable mechanical devices through magnetically tunable bistable elements. *Proc. Natl. Acad. Sci. U.S.A.* **120**, e2212489120 (2023).
37. M. Tan, P. Tian, Q. Zhang, G. Zhu, Y. Liu, M. Cheng, F. Shi, Self-sorting in macroscopic supramolecular self-assembly via additive effects of capillary and magnetic forces. *Nat. Commun.* **13**, 5201 (2022).
38. W. Chang, J. Kim, M. Kim, M. W. Lee, C. H. Lim, G. Kim, S. Hwang, J. Chang, Y. H. Min, K. Jeon, S. Kim, Y.-H. Choi, J. S. Lee, Concurrent self-assembly of RGB microLEDs for next-generation displays. *Nature* **617**, 287–291 (2023).
39. K. J. Russell, D. J. Carter, *Nano-Litz* (The Charles Stark Draper Laboratory, Inc., 2019).
40. W. Ferber, J. Kahnt, G. Jost, Litz Wire For High-Frequency Coils Wound With Water-Repellent Textile Fibres (1974). https://patentimages.storage.googleapis.com/33/bd/72/0cb167f7e0ad2a/US3783179.pdf.
41. J. P. Phillips, *Carbon Nanotube Litz Wire for Low Loss Inductors and Resonators* (2011).
42. J. Eggers, H. A. Stone, Characteristic lengths at moving contact lines for a perfectly wetting fluid: The influence of speed on the dynamic contact angle. *J. Fluid Mech.* **505**, 309–321 (2004).
43. C. Zhu, R. Lu, C. Mei, T. Peng, G. Zhang, Design and simulation analysis of stator slots for small power permanent magnet brushless DC motors. *Int. Trans. Electric. Energy Syst.* **2023**, 1–19 (2023).
44. Y. Niu, R. Zhang, J. Yuan, Flagellar motors of swimming bacteria contain an incomplete set of stator units to ensure robust motility. *Sci. Adv.* **9**, eadi6724 (2023).

Downloaded from https://www.science.org at KIT Library on August 14, 2026

45. M. Byrne, A. Aly, The Surgical Suture. *Aesthet. Surg. J.* **39**, S67–S72 (2019).
46. Y. Kyosev, *Braiding Technology for Textiles* (Woodhead Pub, Waltham, MA, 2014) *Woodhead Publishing Series in Textiles*.
47. A. Duwel, J. LeBlanc, D. J. Carter, E. S. Kim, *Directed Assembly of Braided, Woven or Twisted Wire* (2017).
48. P. Marchand, J. Nolting, D. J. Kent, T. Q. Dinh, H. P. Tran, J. Milburn, J. Thompson, Braiding mechanism and methods of use (2012). https://patents.google.com/patent/US8261648B1/en.
49. S. Giszter, T. G. Kim, A. Ramakrishnan, Method and apparatus for braiding micro strands (2013). https://patents.google.com/patent/US8534176B2/en.
50. Y. Lu, X. Cheng, H. Li, J. Zhao, W. Wang, Y. Wang, H. Chen, Braiding ultrathin Au nanowires into ropes. *J. Am. Chem. Soc.* **142**, 10629–10633 (2020).
51. R. Freeman, M. Han, Z. Álvarez, J. A. Lewis, J. R. Wester, N. Stephanopoulos, M. T. McClendon, C. Lynsky, J. M. Godbe, H. Sangji, E. Luijten, S. I. Stupp, Reversible self-assembly of superstructured networks. *Science* **362**, 808–813 (2018).
52. A. Dasgupta, N. Sori, S. Petrova, Y. Maghdouri-White, N. Thayer, N. Kemper, S. Polk, D. Leathers, K. Coughenour, J. Dascoli, R. Palikonda, C. Donahue, A. A. Bulysheva, M. P. Francis, Comprehensive collagen crosslinking comparison of microfluidic wet-extruded microfibers for bioactive surgical suture development. *Acta Biomater.* **128**, 186–200 (2021).
53. C. S. Haines, M. D. Lima, N. Li, G. M. Spinks, J. Foroughi, J. D. W. Madden, S. H. Kim, S. Fang, M. Jung de Andrade, F. Goktepe, O. Goktepe, S. M. Mirvakili, S. Naficy, X. Lepro, J. Oh, M. E. Kozlov, S. J. Kim, X. Xu, B. J. Swedlove, G. G. Wallace, R. H. Baughman, Artificial muscles from fishing line and sewing thread. *Science* **343**, 868–872 (2014).
54. J. Mu, M. Jung de Andrade, S. Fang, X. Wang, E. Gao, N. Li, S. H. Kim, H. Wang, C. Hou, Q. Zhang, M. Zhu, D. Qian, H. Lu, D. Kongahage, S. Talebian, J. Foroughi, G. Spinks, H. Kim, T. H. Ware, H. J. Sim, D. Y. Lee, Y. Jang, S. J. Kim, R. H. Baughman, Sheath-run artificial muscles. *Science* **365**, 150–155 (2019).
55. S. Chandrasekaran, C. Bowen, J. Roscow, Y. Zhang, D. K. Dang, E. Kim, R. Misra, L. Deng, J. Chung, S. Hur, Micro-scale to nano-scale generators for energy harvesting: Self powered piezoelectric, triboelectric and hybrid devices. *Phys. Rep.* **792**, 1–33 (2019).
56. L. Nan, H. Zhang, D. A. Weitz, H. C. Shum, Development and future of droplet microfluidics. *Lab Chip* **24**, 1135–1153 (2024).
57. F. Guo, P. Li, J. B. French, Z. Mao, H. Zhao, S. Li, N. Nama, J. R. Fick, S. J. Benkovic, T. J. Huang, Controlling cell–cell interactions using surface acoustic waves. *Proc. Natl. Acad. Sci. U.S.A.* **112**, 43–48 (2015).

Acknowledgments: We thank M. W. Faaborg, M. Xiao, and A. Sherif for constructive proofreading of the manuscript. We thank M. Falk and Z. Song for insightful discussions. **Funding:** C.Z. acknowledges support from SINANO startup funding. Y.D. and J.G.K. acknowledge support from the DFG under grant KO 1883/20-1 Metacoils, the German Excellence Intitiative under grant EXC 2082 "3D Matter Made to Order"; J.G.K. acknowledges support from the ERC-SyG (HiSCORE, 951459) and partial support from CRC 1527 HyPERiON.
Author contributions: Conceptualization: Z.L., J.G.K., J.L., Z.M., Y.D., and C.Z. Formal analysis: Z.L., K.L., L.P., J.L., Y.D., and C.Z. Funding acquisition: J.G.K., Y.D., and C.Z. Investigation: Z.L., K.L., L.P., Z.C., and C.Z. Methodology: Z.L., K.L., L.P., Z.C., S.L., J.L., Z.M., Y.D., and C.Z. Data curation: Z.L. and C.Z. Validation: Z.L., Z.M., Y.D., and C.Z. Project administration: S.L., J.G.K., J.L., Z.M., Y.D., and C.Z. Resources: S.L., C.G., J.G.K., J.L., Z.M., Y.D., and C.Z. Software: Z.L. and Y.D. Supervision: S.L., J.G.K., J.L., Z.M., Y.D., and C.Z. Visualization: Z.L. and C.Z. Writing–original draft: Z.L., Y.D., and C.Z. Writing–review and editing: Z.L., K.L., L.P., Z.C., S.L., C.G., J.G.K., J.L., Z.M., Y.D., and C.Z. **Competing interests:** A patent application (CN 202610100394.0) has been filed by Z.L. and C.Z. All other authors declare that they have no competing interests. **Data, code, and materials availability statement:** All data and code needed to evaluate and reproduce the results in the paper are either included in the paper and the Supplementary Materials or available in a Dryad repository (DOI: 10.5061/dryad.sf7m0cgnq). The protocol to generate new materials, including capillary ratchets, floats, fibers, and braids, are available in Materials and Methods.

Submitted 27 November 2025
Accepted 18 May 2026
Published 3 July 2026
10.1126/sciadv.aed5495

Downloaded from https://www.science.org at KIT Library on August 14, 2026

Science Advances

Capillary ratchets activated by interfacial flows for versatile torque generation and microassembly

Zhe Li, Keliang Liu, Lida Pan, Zhangyuan Cheng, Shuxian Li, Chengchen Guo, Jan G. Korvink, Jiadong Li, Yongbo Deng, Zongmin Ma, and Cheng Zeng

Sci. Adv. **12** (27), eaed5495. DOI: 10.1126/sciadv.aed5495

Downloaded from https://www.science.org at KIT Library on August 14, 2026

View the article online
https://www.science.org/doi/10.1126/sciadv.aed5495
Permissions
https://www.science.org/help/reprints-and-permissions

Use of this article is subject to the Terms of service

Science Advances (ISSN 2375-2548) is published by the American Association for the Advancement of Science. 1200 New York Avenue NW, Washington, DC 20005. The title *Science Advances* is a registered trademark of AAAS.

Copyright © 2026 The Authors, some rights reserved; exclusive licensee American Association for the Advancement of Science. No claim to original U.S. Government Works. Distributed under a Creative Commons Attribution NonCommercial License 4.0 (CC BY-NC).